Effects of Bubble Coalescence Dynamics on Heat Flux Distributions Under Bubbles

Bi Jingliang, Lin Xipeng, and David M. Christopher
Key Laboratory for Thermal Science and Power Engineering of Ministry of Education, Dept. of Thermal Engineering, Tsinghua University, Beijing 100084, China

DOI 10.1002/aic.13932
Published online October 15, 2012 in Wiley Online Library (wileyonlinelibrary.com).

Bubble coalescence events and single bubble nucleation, growth, and departure were observed with a charge-coupled device (CCD) camera synchronized with a high-speed data acquisition system measuring the heat fluxes at different positions underneath the bubble. Four different kinds of coalescence events took place with characteristic heat flux signatures for each type of event. The heat transfer measurements under four typical heaters representing different positions under the bubble showed very different heat flux characteristics during each ebullition cycle. The results show that transient conduction due to the movement of the contact line during bubble interactions, sliding, stretching, and oscillating is the main mechanism resulting in the high heat transfer rates during coalescence. Fast evaporation of the liquid layer trapped between the two bubbles and higher heat fluxes near the contact line as the microlayer evaporated also generate high heat flux spikes but have less influence due to their short duration and small influence area. © 2012 American Institute of Chemical Engineers *AIChE J,* 59: 1735–1745, 2013
Keywords: bubble coalescence, heat flux, transient conduction, boiling

Introduction

Bubble coalescence is an important phenomenon in boiling and other chemical processes. There have been many studies to investigate the mechanisms and characteristics of the bubble dynamics during coalescence[1–7] with experimental, numerical, and analytical studies. However, in most studies, the heating surface was quite large compared with the bubble that smears out the details of the heat transfer process making accurate analyses of the effects of the different mechanism more difficult.

Many models have been proposed to predict nucleate boiling heat transfer with various studies used to test the validity of each model.[8–14] Mikic and Rohsenow proposed the transient conduction model, which assumed that a departing bubble scavenged away the superheated layer surrounding the bubble in an area twice the bubble departure diameter, which allowed the colder bulk liquid to contact the surface. This model predicted a very large heat transfer rate immediately after the bubble departed from the surface over an area about twice the bubble departure diameter. The heat transfer during nucleation and bubble growth was assumed to be negligible. Moghaddam and Kiger[15,16] used a set of temperature sensors to measure the wall temperature to calculate the heat transfer rates for three different mechanisms. They found that the transient conduction heat transfer was significant in the bubble contact area, mostly prior to bubble departure. Christopher et al.[17] found that the heat transfer due to the sliding of bubbles is significantly larger than the heat transfer due to evaporation under bubbles on microwires, which also implies that transient conduction contributes more to the boiling heat transfer than microlayer evaporation.

The coalescence of two bubbles on nearby nucleation sites has also been studied by various researchers. Zhang and Shoji[18] investigated the average bubble departure frequency from two artificial cavities on a thin silicon surface for different dimensionless cavity spacings, which is the ratio of the cavity spacing to the average bubble departure diameter. Three significant factors found to affect the nucleation site interactions were hydrodynamic interactions between bubbles, thermal interactions between nucleation sites and horizontal and declining bubble coalescence. Bonjour et al.[19] used artificial nucleation sites to obtain boiling curves while increasing the heat flux up to the heat flux leading to the first parasitic nucleation site becoming active. They obtained boiling curves for various intersite distances with their results showing that coalescence improved the heat transfer coefficient, which was attributed to supplementary microlayer evaporation. Siedel et al.[20] used two artificial nucleation sites to obtain two bubbles growing side by side. The bubble volume was plotted as a function of time, and an experimental growth law was proposed. Lateral coalescence was visualized with the results tending to show that lateral coalescence does not have a great impact on the vapor production during merging and that the macrolayer between the bubbles is removed because of capillary effects rather than by vaporization. Coulibaly et al.[21] found that the macrolayer between coalescing bubbles was removed only during fast coalescence events with coalescence numbers much less than 1.

Correspondence concerning this article should be addressed to D. M. Christopher at dmc@tsinghua.edu.cn.

Microheater arrays have been used in various studies to generate bubbles and to determine the heat fluxes under the bubbles. A 1 × 1 mm^2 heater array was used by Demiray and Kim[22] to obtain time and space resolved data under nucleating bubbles with low and high subcoolings for single bubbles. They observed oscillating bubbles and sliding bubbles in highly subcooled boiling as was observed by Christopher et al.[23] on microwires. Their heat transfer measurements and a simple model for the heat transfer under sliding and oscillating bubbles indicated that transient conduction during the rewetting process was dominant. Chen and Chung[24] used two heaters (0.27 × 0.27 mm^2) to produce two individual bubbles side by side. They recorded two major heat flux spikes for each typical boiling coalescence cycle. They determined that the first spike corresponded to bubble nucleation and the second corresponded to the coalescence of the two bubbles. Comparison with single bubble results showed that the heat transfer was greatly enhanced by the coalescence.

Experimental System

Heater design and control

The heaters used in the experiment to study boiling coalescence are shown in Figure 1. The heaters were sorted into Group B and Group E with 10 heaters in Group B and 12 heaters in Group E. Some of the heaters between Groups B and E were not activated for various reasons, so the surface in this area provided what was essentially an insulated surface. The two heater groups were on a 96 microheater array such as has been used in other studies.[23,25] The complete 96 heater array was 1 × 1 mm^2 in size. The heaters were formed by sputtering titanium and aluminum onto the entire surface of a 500-μm thick SiO_2 substrate to form a 0.3-μm thick titanium layer followed by a 1.0-μm thick aluminum layer. A layer of photoresist was deposited on the surface and patterned to define the wire and pad geometries. The Ti/Al layers were then dry etched to form the heaters, and the Ti/Al leads to bonding pads on the outside edges of the chips. Then, the heater geometries were patterned with a second photoresist layer with the aluminum then removed from the heaters by wet etching to form the serpentine Ti heaters. Finally, the whole wafer was divided into many chips, each containing one heater array. The wires and the spacings between the wires were both 7-μm wide. The heater array was mounted on a printed circuit board (PCB) board with each heater controlled by the Wheatstone bridge circuit shown in Figure 2. All 96 Wheatstone bridge circuits were mounted on four PCB boards with connections to a computerized control system.

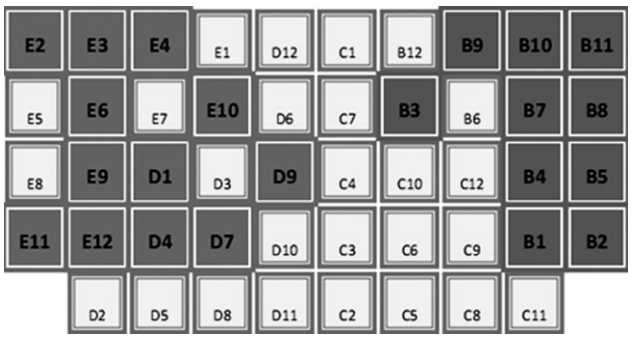

Figure 1. Heater layout (dark colors represent the working heaters).

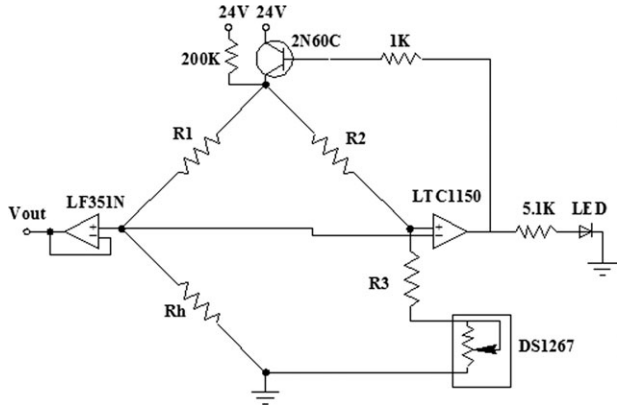

Figure 2. Control circuit (Wheatstone feedback bridge).

The experiment used FC-72 as the working fluid, because this dielectric fluid will not damage the heaters. The saturation temperature of FC-72 is 56°C at 1 atm.

The control circuit shown in Figure 2 contained a Wheatstone bridge with an LTC1150 amplifier to amplify the bridge imbalance. The amplified signal was then fed into the 2N60C power transistor to control the power into the bridge. When the bridge was balanced

$$R_1/R_h = R_2/(R_3 + R_v) \tag{1}$$

The heaters were made of titanium, so their resistance was linearly related to the temperature as

$$R_h = R_0[1 + \alpha(T - T_0)] \tag{2}$$

The resistance of the variable DS1267 resistor, R_v, was set to the value needed to give the desired heater resistance, R_h, for the desired temperature. If the circuit was not balanced, the LTC1150 amplifier output a signal to the 2N60C power controller to increase or decrease the voltage into the bridge to increase or decrease the power into the heater until the heater resistance balanced the circuit. This very fast feedback accurately controlled the heater temperature to the set temperature corresponding to the DS1267 set resistance.

Data acquisition and test procedure

The experimental system used in the boiling experiments is shown in Figure 3. The pressure in the test section was controlled by the pressure rig attached to the boiling pool and measured by a pressure transducer. The bulk liquid temperature was measured by a K-type thermocouple with the

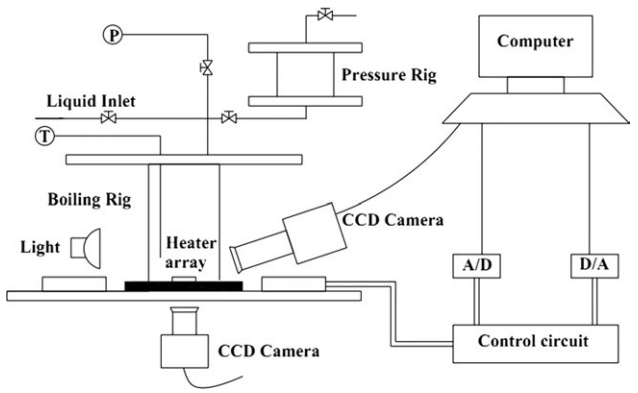

Figure 3. Experimental setup.

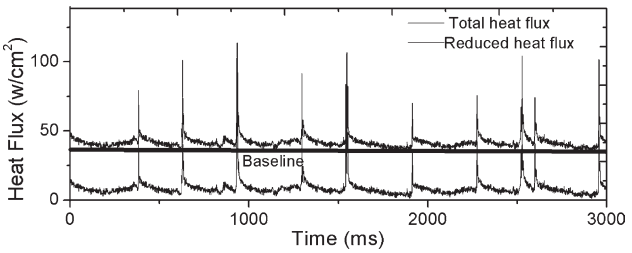

Figure 4. Example of the heat flux data base line method.

heater temperatures controlled to their desired values by the control circuit. The bubble behavior was recorded by a high-speed CCD camera at 1000 fps, whereas the voltages across the heaters were measured by a Measurement Computing USB1616-HS high speed data acquisition system with a sampling rate of 1000 Hz per channel. The heat flux was then computed from the voltage across each heater as

$$q'' = \left(V^2/R\right)/A \tag{3}$$

The bulk liquid temperature in the experiment was 25°C, and the pressure in the boiling rig was 68 kPa, which corresponds to a saturation temperature of 46°C. The heaters were set to 120°C. The two groups of heaters were heated separately to observe the heat transfer characteristics during bubble nucleation and departure for each single bubble. Then, they were heated at the same time to form two adjacent bubbles that could coalesce.

Data reduction and uncertainty analysis

The heat flux due to the bubble coalescence and motion is the main concern in this study, so the heat flux due to conduction to the substrate and the heat loss to the vapor or liquid above the heater with no bubble motion was subtracted from the total heat flux curves obtained from Eq. 3. These conduction and natural convection heat fluxes were then determined using a similar method to that used by Demiray and Kim.[22] A baseline was selected as the lowest point on the total heat flux curve to represent the heat flux due to conduction and heat loss to the vapor or liquid above the heater. The heat fluxes due to the bubble dynamics were then taken as the heat flux increase above this baseline.

An example of the data reduction method is shown in Figure 4. The baseline was obtained by drawing a horizontal line tangent to the lowest heat flux regions on the curve. Then, the baseline was subtracted from the total heat flux curve to get the net change of the heat flux due to the presence of the bubbles. Most of the resulting heat flux changes are positive with a few being slightly negative due to uncertainties in the measurements.

After the heater calibration, the uncertainties in the temperatures indicated by the heater were approximately 0.3°C. The uncertainty in the heat flux measurements was a function of the error in the voltage measurements by the USB 1616HS, the uncertainty in the heater area that was very small and the uncertainty in the heater resistance that was accurate to within 0.5%. The uncertainty in the voltage measurements was less than 2% due to uncertainties in the measurement equipment and the electronic circuits. The uncertainty of the heater area was about 0.2%. The heat flux calculations then had an uncertainty of less than 4.8% due to the measurement inaccuracies in the circuitry and data acquisition system. The bubble departure diameter was analyzed using image analysis software that gave uncertainties in the bubble size measurements of about 2%.

Results and Discussion

Bubble coalescence effects on heat flux distribution under bubbles

The two groups of heaters were heated together to get bubbles at a surface temperature of 120°C with a bulk liquid temperature at 25°C, which gives a surface superheat of 74°C and a liquid subcooling of 11°C. High-speed movies of the bubble dynamics at 1000 frames per second were synchronized with high-speed heat flux measurements on various heaters during numerous bubble ebullition cycles.

As the heating surface was at a constant surface temperature, the surface heat flux reflects the bubble heat transfer mechanisms during coalescence events. Analysis of the heat fluxes for all the heaters showed that different heaters had different heat flux characteristics during the coalescence events. These heaters can be sorted into four kinds according to their heat flux characteristics. Four typical heaters are used here to represent heaters at different positions. The geometry of the four heaters is shown in Figure 1. These four heaters are on a straight line on the heater array at different positions under the bubbles.

The heat flux characteristics for the four heaters are shown in Figure 5. B8 has many high heat flux spikes along with some long high-heat-flux regions. B3 has two close spikes corresponding to each heat flux spike on B8 and also has many heat flux spikes during the high heat flux region on B8. E10 has fewer spikes than other heaters, and its spikes last for very short times. E6 also has some high heat flux regions, but the heat fluxes in these regions were not as high as the spikes elsewhere.

To understand the mechanisms driving the heat flux variations on each heater, the bubble dynamics during the coalescence events were observed with the frames synchronized with the heat flux measurements. The specific heaters in contact with the contact line were identified by careful analysis of the pictures from underneath the heater. Analysis of the synchronized bubble images and heat flux data showed that

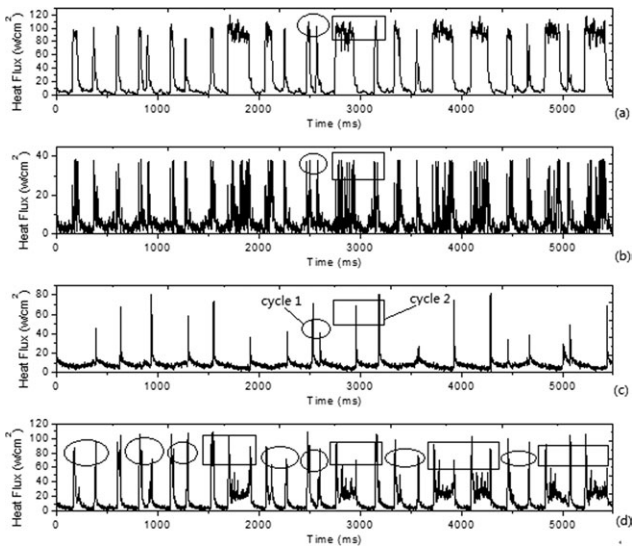

Figure 5. Heat flux plots during coalescence events (a) B8, (b) B3, (c) E10, and (d) E6.

coalescence of two bubbles of almost the same size as well as coalescence of bubbles having different sizes. In this article, the first case is called same size coalescence, whereas the second case is called different size coalescence. The coalescence starts with two bubbles growing until the bubble interfaces contact each other. The two interfaces merge into one and both sides move toward the middle. The bubble shape oscillates several times as the bubble becomes more circular with a relatively smooth surface. This big bubble then lifts off due to its larger buoyancy leaving two new bubbles growing on the two groups of heaters. However, sometimes this bubble does not immediately depart, but instead stays on the surface until a small bubble formed on the other heater group grows sufficiently to coalesce with this big bubble in a different size coalescence event.

After the different size coalescence, the new big bubble departed the surface immediately, so the time from different size coalescence to departure was usually very short, lasting 30–50 ms, while the time from same size coalescence to departure was either short or long depending on the cycle. Sometimes, after the same size coalescence, the new large bubble did not depart immediately but remained on the surface for a long time to departure, which is termed a long coalescence-to-departure process. These long processes lasted about 200 ms, whereas the short processes lasted only about 50 ms.

Four kinds of typical coalescence events occurred with same size coalescence without departure, different size coalescence, same size coalescence with a long time to departure, and same size coalescence with immediate departure. The bubbles formed after the different size coalescence always departed, whereas the bubbles formed in a same size coalescence event either departed or then coalesced with a smaller bubble.

Thus, the bubble dynamics had two kinds of cycles:

- Departure–Same size coalescence–Different size coalescence–Departure (Cycle 1);
- Departure–Same size coalescence–Departure–Same size coalescence–Departure (Cycle2).

Cycle 1 is marked by ellipses in Figure 5, whereas Cycle 2 is marked by rectangles. The two cycles alternated in the experiment as shown in Figure 5d.

In addition, the observations and measurements show that each spike on E10 corresponds to a bubble departure event in the bubble images. The spikes for B8, B3, and E6 either correspond to a departure or a coalescence event. The high heat flux regions on B8 correspond to long coalescence-to-departure processes. The results show that bubble coalescence greatly enhances the heat transfer on the heating surface. The coalescence also results in bubble departure that also greatly enhances the heat transfer. The heat flux spikes during the coalescence events are also as high as the spikes during departure events.

Analysis of the heat flux characteristics and the bubble dynamics corresponding to the heat flux variations showed that different heat flux characteristics on different heaters depended on the heater location relative to the bubbles in the coalescence events. Two typical cycles were selected from Figures 5a–d to be analyzed in Figure 6. The heat flux plots for a same size coalescence without departure, a different size coalescence, a same size coalescence with a long time to departure, and a same size coalescence with immediate departure are shown in order in Figure 6 for different heaters.

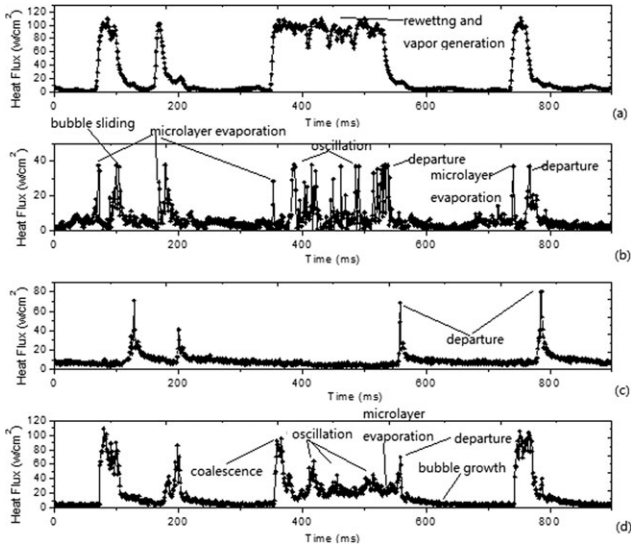

Figure 6. Heat flux plots for four typical coalescence processes (a) B8, (b) B3, (c) E10, and (d) E6.

Time zero here corresponds to 2400 ms in Figure 5.

B8 is on the edge of the heater array, and the bubble images show that after coalescence, B8 was always outside of the dryout area under the bubble and exposed to the liquid. Thus, the region represented by B8 is called the wetted region. Single bubbles kept growing and then quickly condensing on B8 and adjacent heaters until one bubble finally began to grow steadily on them. During this process, B8 experienced high heat fluxes until the steady growth of the small bubble. The high heat flux was due to microlayer evaporation during the fast growth of the small bubbles and transient conduction after the bubble condensed.

B3 is between two growing bubbles and on the edge of the dryout area of the bubble formed after coalescence, so that some of B3 is in the dryout area and some is wetted. Thus, the region represented by B3 is often rewet during the contact line oscillations. There are two major spikes on heater B3 during each short coalescence event as shown in Figure 6b with the first spikes at about 70, 168, and 740 ms and the second spikes at about 99, 178, and 766 ms. The first spike is due to fast evaporation of the liquid layer trapped between the two coalescing bubbles, whereas the second spike is due to bubble departure. During the long coalescence-to-departure processes, a spike also occurs before the high heat flux region with the first spike due to the fast evaporation of the liquid layer trapped between the two coalescing bubbles. The first heat spike is observed, because B3 is between the two bubbles outside of both bubbles' dryout areas, so when the two bubbles coalesced, there was a liquid layer trapped between the two coalescing bubbles on top of B3. The rapid vaporization of this liquid layer then resulted in a heat flux spike. This is similar to rapid evaporation of the microlayer first suggested by Moore and Mesler[11] and verified by Hendricks and Sharp,[12] Cooper and Lloyd,[13] and Bonjour et al.[19] for single bubbles. Chen and Chung[24] and Coulibaly and Christopher[21] also measured large heat flux spikes during coalescence with the spikes attributed to evaporation of the liquid layer that was initially between the bubbles and then became trapped under the bubbles as they coalesced. The other heat flux spikes in the plots are due to the transient conduction and fluid motion during the deformation, necking, and departure processes.

E10 is in the dryout area during bubble growth and is still in the dryout area during coalescence. The region represented by E10 is then called the dryout region. Only when the bubble starts to neck and the contact line shrinks to the center is E10 finally rewet. A small bubble then immediately forms on E10 with a very short spike, as the heater is blanketed with vapor and the heat flux quickly decreases. Therefore, there is only one spike on E10 during an ebullition cycle corresponding to the bubble departure. The spike in the coalescence-without-departure event is a special case as the bubble slides farther than usual from E10 and E10 is out of the dryout area. E10 is then rewet, so the heat flux increases sharply at this moment. This clearly shows that transient conduction, as the heater is rewet by the cooler liquid, is the most important mechanism for the high heat transfer rates.

The observations also show that the contact line moves across E6 during the coalescence to departure processes with most of E6 outside of the contact line. The microlayer along the oscillating contact line lies on E6, so E6 could be called moving microlayer region. E6 usually has two or three spikes in one ebullition cycle due to the oscillation of the contact line position.

The contact line crossed both E6 and B3, but the amount of heater area exposed to the dryout region differed. Most of B3 was in the dryout area, so the oscillations of the contact line caused rewetting of a larger area on the heater. The heat flux spikes shown in Figure 6b occurred many times as more of the heater was partially rewet, with low heat fluxes for the rest of time when the heater was mostly covered by the dryout region. Only a small part of E6 was in the dryout area, and the contact line did not move as much on E6. Thus, the heat flux remained relatively high and steady due to evaporation near the contact line as shown in Figure 6d.

Two typical coalescence events are analyzed in detail in the next two next sections to describe the heat-transfer mechanisms. One is the same size coalescence with a long time to departure, and one is the different size coalescence. The heat fluxes for the different heaters are analyzed together with the bubble dynamics observed from both the bottom and the side.

Effect of bubble dynamics on the localized heat flux characteristics during a typical same size coalescence

The typical same size coalescence with a long time to departure usually includes the bubble growth, bubble coalescence, deformation and oscillations of the bubble, and the bubble departure as shown in Figure 6d. For B8, the heat flux shown in Figure 6a is always high during the long coalescence-to-departure processes, B3 has several spikes, and E6 has two high spikes at the beginning and at the end of the process with relatively lower fluxes in between. E10 has only a short spike at departure with very low heat fluxes at other times.

Figure 7 shows the bubble dynamics during a typical long time same size coalescence process shown as both bottom and side views, where the starting time in Figure 7 corresponds to 346 ms in Figures 6a–d. The bright part in the center of the bubble in Figure 7a is the dryout area, whereas the large dark outer circle is the bubble outer diameter in the horizontal plane. Coalescence occurs from 346 to 351 ms in Figure 7, forming a bubble with a relatively irregular surface as shown in Figure 7b. Then, the coalesced bubble contracts toward the middle in the axial direction from 351 to 358 ms. This contraction right after coalescence is caused by the interfacial surface tension pulling the two coalesced bubbles into a sphere. From 359 to 367 ms, the large coalesced bubble deforms in the opposite direction with stretching in the axial direction and contracting in the perpendicular direction as seen in Figure 7a beginning at 359 ms. The bubble surface was still irregular during this process due to the rapid motion. This deformation reversed directions several times because of the fluid momentum causing the bubble to compress too far in one direction such as the axial direction after 358 ms seen in Figure 7, whereas the interface in the other direction is overexpanded. By 359 ms, the surface tension forces and the pressure in the bubble have caused the interface motion in the axial direction to reverse direction and begin moving outward just as the interface motion in the perpendicular direction is reversing direction and moving back inward. From 368 to 375 ms, the bubble shrinks in the axial direction while moving to the left side of the heater array, as can be clearly seen in Figure 7a. The bubble surface became more regular after this process as shown in Figure 7b. From 376 to 386 ms, the bubble continued moving to the left as the length in the axial direction increased. The shrinking and expanding in both the axial and the perpendicular directions, which was repeated many times before the bubble shape became steady, illustrates the shape oscillations caused by the varying surface tension forces, liquid momentum, and pressure inside the bubble. From 386 to 422 ms, the bubble length did not change much in either direction as the bubble surface became fairly steady. After 422 ms, the bubble slowly grew until 533 ms, when the big bubble started necking and a small bubble formed on the Group B heaters on the right side. At 556 ms, the bubble departed.

Figure 7a shows that after 349 ms, B8 was outside the dryout area with very small bubbles repeatedly generated and condensed on B8 until a small, steady bubble formed on B8 at about 534 ms. Thus, B8 was repeatedly rewet with rapid vapor generation with much of the vapor generated by microlayer evaporation of the many new microlayers formed under the new bubbles. The heat flux was then very high on B8 from 349 to 534 ms as shown in Figure 6a with this high heat flux region corresponding to the deformations seen from the same time region in Figure 7.

The first spike on B3 at 346 ms in Figure 6b occurred as the two bubbles first coalesced as shown in Figure 7. This spike was due to the fast evaporation of the liquid layer trapped between the two coalescing bubbles as explained in the previous section. E10 then has many heat flux spikes from 376 to 533 ms. The synchronized bubble images show that at 376 ms, the larger bubble begins to move toward the Group E heaters, which creates a heat flux spike on B3. Most of B3 was rewet from 379 to 384 ms as shown in Figure 7a, which corresponds to a large spike observed in the heat flux plot on heater B3 as shown in Figure 6b. At 389 ms, the bubble stopped moving toward the Group E side. From 386 to 422 ms, the bubble was deforming and moving slowly toward the middle. During this process, the contact line kept changing shape as the bubble continued to deform with some contracting and expanding along the contact line, with the shrinking contact line and dryout area on B3 causing repeated spikes in the heat flux. After 423 ms, the bubble deformation slowed, but B3 was still on the edge of the contact line and was rewet several times resulting in several small heat flux spikes. At 533 ms, B3 was totally rewet and the necking process began.

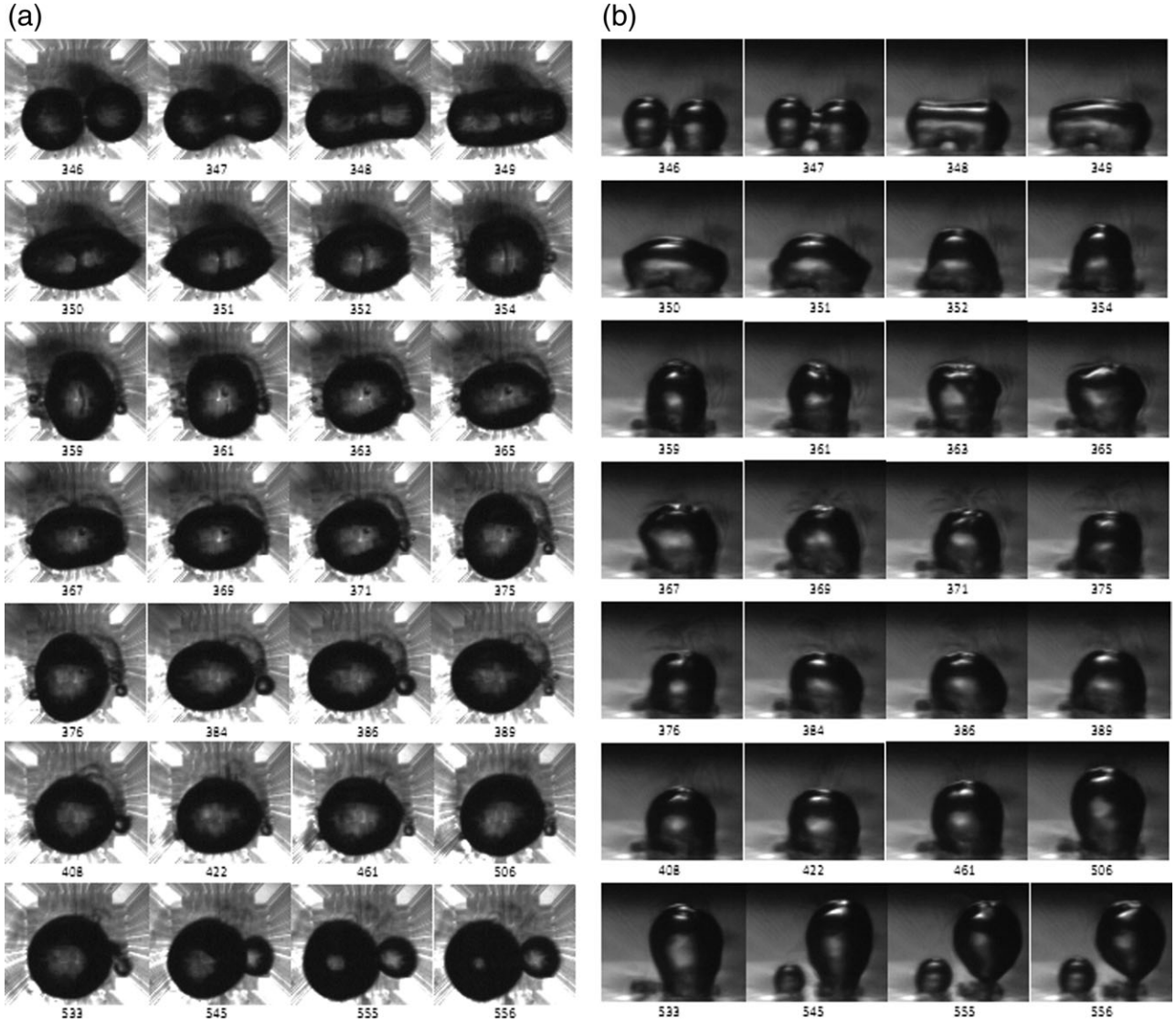

Figure 7. Typical long time same size coalescence process (numbers indicate the time in milliseconds).

(a) Bottom view and (b) side view.

The bubble started necking at 533 ms, with E10 rewetted from 553 to 555 ms. A small bubble then formed on E10 with E10 and then covered by the dryout area. The rewetting of E10 from 553 to 555 ms shown in Figure 7a corresponds to a heat flux spike that only lasted for several milliseconds as shown in Figure 6c.

When the two bubbles first coalesced, E6 was partly in the dryout area as shown in Figure 7a. From 351 ms, the bubble began shrinking, and E6 was mostly or completely rewet and the heat flux in Figure 6d increased. Then, from 359 ms, the bubble started stretching in the axial direction and the dryout area moved back to cover part of E6 at 363 ms. E6 was mostly wetted from 351 to 363 ms, which can be clearly seen by the large heat flux peak in Figure 6d. The contact line was then across E6 with only a small part of E6 in the dryout area. The oscillations of the contact line were fairly small here and did not affect the size of the dryout area on E6 much with most of E6 covered by the microlayer, so the heat flux during this process remained relatively high, higher than during the bubble growth period when E6 was totally covered by the dryout region. This higher heat flux region is mostly caused by microlayer evaporation along the oscillating contact line. This example shows that the high microlayer evaporation can last for relatively long times, such as 190 ms in this case, unlike the much shorter times of 2 ms observed by Moore and Mesler.[11] At 408 ms during the deformation process, E6 was totally rewet for several milliseconds resulting in a higher heat flux at that time in Figure 6d. The oscillation of the contact line also twice caused rewetting of a small area, which can be seen as two small spikes that are higher than the higher heat flux region after 408 ms. The bubble started to lift off from 554 ms and E6 was totally rewet, resulting in a large spike in Figure 6d.

Effect of the bubble dynamics effects on the localized heat flux characteristics during a typical different size coalescence

Typical pictures of the bubble dynamics during different size coalescence events are shown in Figure 8. At 0 ms, the bubble interfaces touch each other and by 2 ms, the two bubble interfaces are merged into one smooth interface.

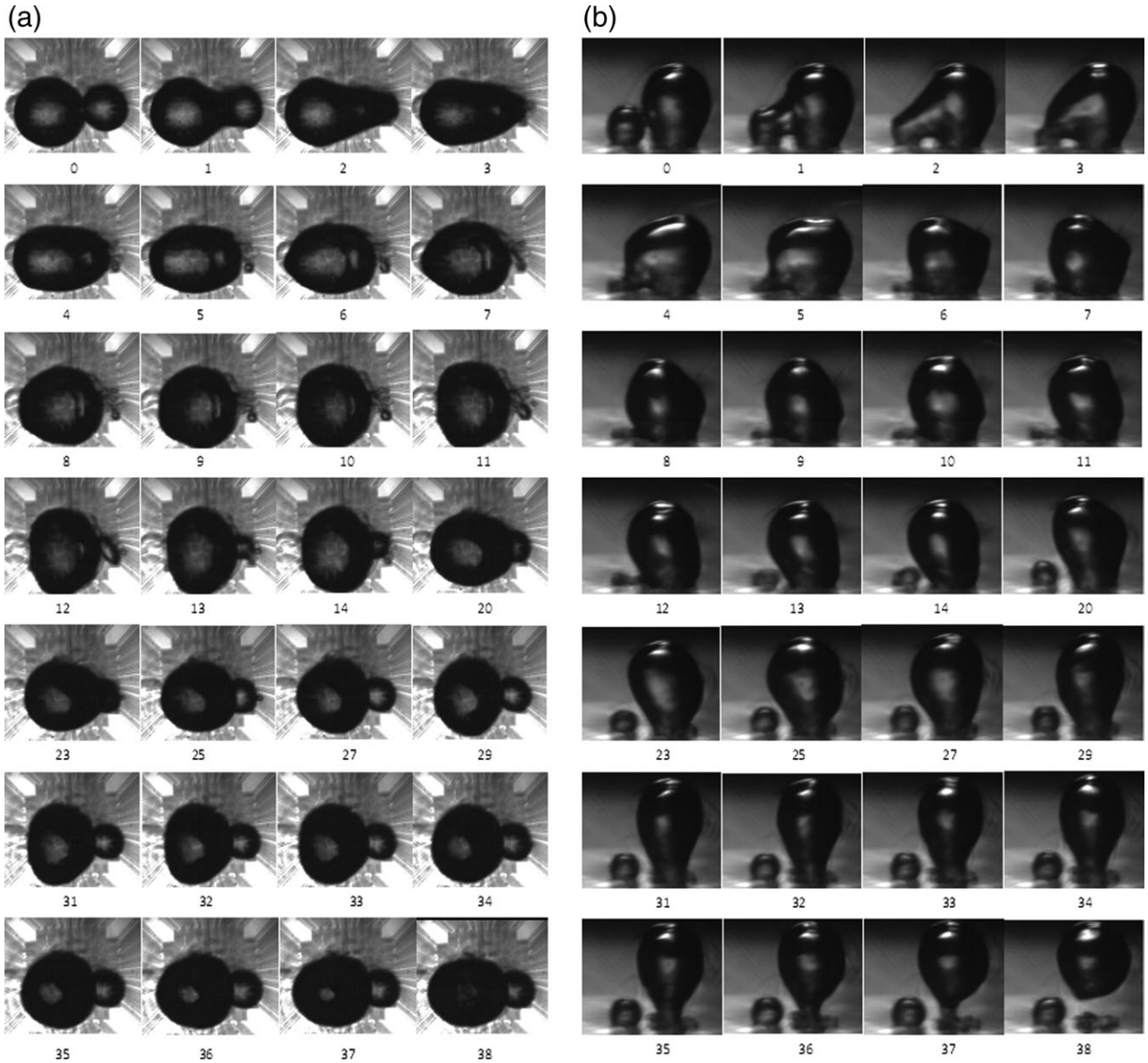

Figure 8. Typical different size coalescence process.

(a) Bottom view and (b) side view.

At 3 ms, the smaller part of the merged bubble on the right (generated on the Group B heaters) begins to move toward the larger part on the left (generated on the Group E heaters). At 6 ms, the left part of the bubble also begins to shrink toward the middle resulting in shrinking of the contact line. Heaters near the contact line, represented by E6, are rewet during this process. From 3 to 12 ms, the length of the combined bubble in the axial direction keeps shrinking, while the length perpendicular to the axial direction is stretching as the surface tension pulls the interface toward a spherical shape. At the same time, heaters under the edge of the bubble, represented by B8, are exposed to the liquid with small bubbles forming and condensing several times on the surface at that location. Two small bubbles form on the right side at 11 ms and quickly combine at 12 ms. At 13 ms, the smaller bubble starts to grow steadily on B8 and adjacent heaters. From 14 ms, the dryout area starts to move away from the smaller bubble due to the liquid motion caused by the fast growing smaller bubble pushing the larger bubble away. The top part of the larger bubble keeps growing, leading to an increase of the projected bubble outer diameter in the horizontal direction as shown in Figure 8b from 20 to 29 ms. At the same time, the top of the larger bubble shifted away from the smaller bubble with the bubble finally shifting from inclined to vertical. This can be seen in Figure 10 from 20 to 27 ms as the dryout region and the projected bubble outer interface shift to the left away from the smaller bubble on the right. The smaller bubble on the right does not become big enough during this time to contact the interface of the larger bubble but does push liquid toward the underside of the larger bubble that pushes the larger bubble up. The large bubble starts lifting away from the surface and necking at 29 ms with the dryout area quickly shrinking until the bubble departs at 38 ms.

The heat flux variations during the difference size coalescence process are explained in the following based on the heat flux characteristics shown in Figure 9. The times in Figure 9 correspond to the times in Figure 8.

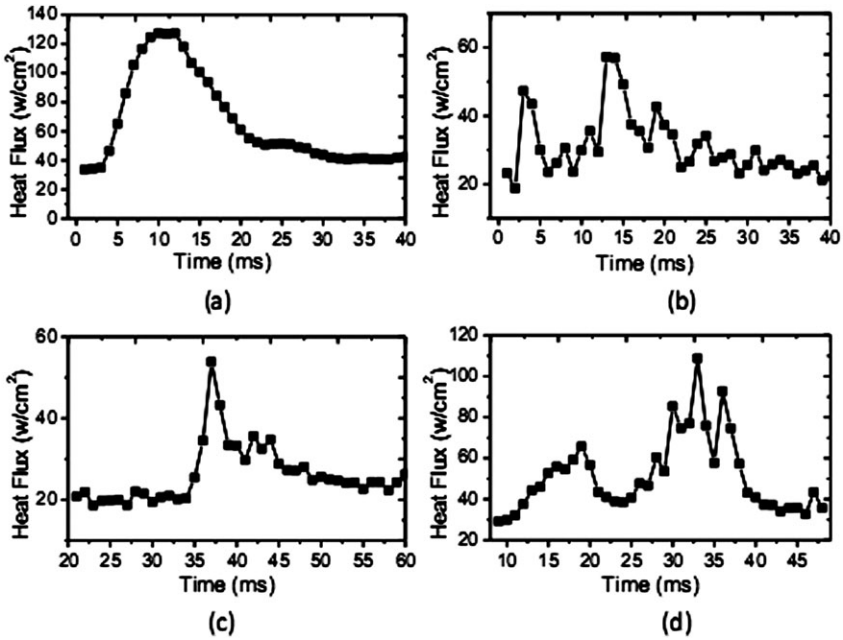

Figure 9. Heat flux plots during a typical different size coalescence (a) B8, (b) B3, (c) E10, and (d) E6.

B8 is partially in the dry-out area under the smaller bubble at 0 ms as shown in Figure 8a. Due to the coalescence at 3 ms, the smaller bubble is pulled toward the bigger bubble and B8 is rewet. Therefore, the heat flux quickly increases beginning at 3 ms as shown in the heat flux plots in Figure 9a and then starts decreasing at about 12 ms as the fluid temperature increases near the wall. The vapor region keeps growing on B8 and adjacent heaters until 13 ms, when the fluid is sufficiently superheated to allow formation of a small bubble on B8 and adjacent heaters. As the smaller bubble grows, the dryout area expands as shown in Figure 8a. The heat flux continues to decrease with time as the dryout area increases.

At 0 ms, B3 is close to but outside of the contact line of the small bubble as shown in Figure 8a. From 1 to 3 ms, the liquid on top of B3 is trapped between the two bubbles. The heat transfer increases rapidly from 1 to 3 ms due to the rapid vaporization of the thin liquid layer trapped under the bubble as shown by the small spike in the heat flux plot in Figure 9b. By 4 ms, the vapor has covered B3 in Figure 8a and the heat flux in Figure 9b has decreased. At 13 ms, B3 is again totally rewet by the bubble deformation, and the heat flux has again increased as the cold liquid contacts the heater with rapid transient conduction in the substrate.

E10 is always in the dryout area during the coalescence and the subsequent deformations until E10 is rewet during the necking process beginning at about 34 ms and is totally rewet by 37 ms as shown by the spike at 37 ms in the heat flux plot in Figure 9c.

E6 is in the dryout area from 0 to 5 ms. At 6 ms, the bubble starts to shrink toward the middle with E6 partially rewet at 14 ms. The heat flux is not very high in Figure 9d indicating only part of the heater was rewet with the contact line crossing heater E6 as can be seen in Figure 8a. At 29 ms, the bubble starts necking and the contact line moves back and forth across the heater causing the heat flux to increase. E6 is totally rewet at 34 ms with a high heat flux spike at that moment.

Analysis of the heat transfer enhancement due to coalescence and departure

The correlation of the bubble dynamics with the heat flux measurements shows that the bubble sliding and deformation resulting from the coalescence of the two bubbles greatly increases the heat flux, so transient conduction after rewetting is the main mechanism for the increased heat transfer after bubble coalescence. Microlayer evaporation was also important in some cases, but only for very short times over very small areas as indicated by the various microlayer models.[25–27] Evaporation of the liquid regions trapped between coalescing bubbles is also important, but these did not result in heat fluxes as large as for the transient conduction and did not occur as often as the rewetting and transient conduction.

The heat transfer enhancement during bubble coalescence with nucleate boiling can be divided into two parts. First, the natural convection was enhanced by the liquid motion caused by the bubble growth. This heat flux enhancement was quantified by subtracting the natural convection when there was no bubble from the heat flux as the bubble was growing. This part of the heat flux is shown in Figure 10 for the different heaters as q'' (bubble growth). Second, the bubble coalescence also greatly increases the heat flux, with this

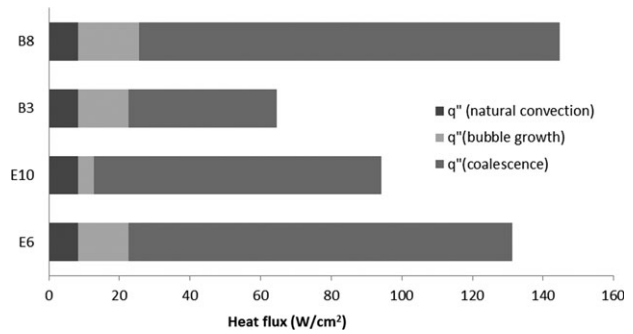

Figure 10. Heat flux enhancement during coalescence events.

increase shown in Figure 10 as q'' (coalescence) due to the transient conduction and microlayer evaporation. Bubble coalescence, sliding, and deformation results in movement and oscillation of the contact line, which causes rewetting of all the heaters. This part of the heat flux enhancement caused by liquid rewetting was all due to transient conduction. Fast microlayer evaporation also occurred as small bubbles kept growing and quickly condensing on B8. The liquid layer trapped between two coalescing bubbles results a short heat flux spike on B3. Oscillation of the contact line also results in additional microlayer evaporation on E6.

The natural convection heat flux when there was no bubble was 8.3 W/cm^2 using the standard correlation for natural convection above a horizontal heated surface

$$Nu = 0.54(Gr\,Pr)^{1/4}, \quad 10^4 \le Gr\,Pr \le 10^7 \tag{4}$$

The heat flux increases due to the bubble growth for B8 and E6 were larger than the increases for B3 and E10, as can be seen in Figure 10, because the heaters outside of the contact line region were easily influenced by the liquid motion caused by the bubble growth. E10 was in the dryout area, so the heat flux increase due to bubble growth was only 4.5 W/cm^2 on E10. B8 was also outside the contact line and the heat flux enhancement was larger, reaching 17.2 W/cm^2. B3 and E6 were partially in the dryout area for most of the time, so the heat flux increases were both 14.3 W/cm^2 on these two heaters.

The heat flux enhancement due to bubble coalescence was much larger than the enhancement due to bubble growth, as can be seen from Figure 10. The largest increase occurred on heater B8, with the heat transfer reaching 119.1 W/cm^2, 87.4% of the total heat flux increase for this nucleate boiling scenario. B3 had the smallest heat flux increase of 42.0 W/cm^2, because it was mostly covered by the dryout area with very little rewetting. Most of the surface areas of E6 and E10 were rewet, so the heat fluxes on those heaters reached 108.7 and 81.3 W/cm^2.

The two groups of heaters were also heated separately to get single bubbles without coalescence at the same surface superheat and liquid subcooling. Single bubble ebullition cycles on the Group E heaters are analyzed here. As could be seen in the bubble pictures, the contact line location oscillated several times before the bubble on the Group E heaters departed. The heat flux plots corresponding to the bubble dynamics at this time are shown in Figure 11. E6 and E10 were used to represent heaters under the dryout area and near the contact line. In Figures 11a,b, the bubble

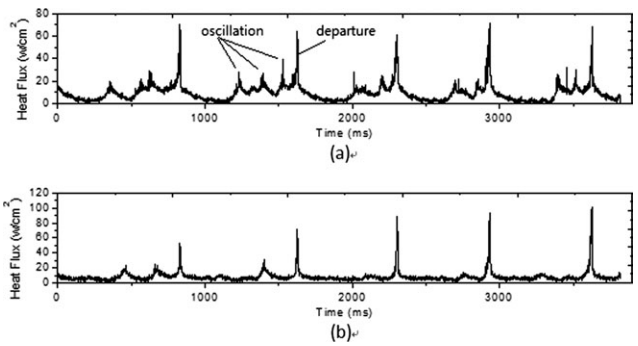

Figure 11. Heat flux plots for single bubble growth.

(a) E10 and (b) E6.

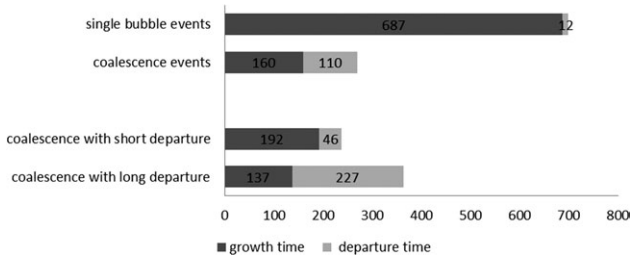

Figure 12. Comparison of average growth and departure times for multiple coalescence and single bubble events (the numbers on the abscissa indicate the time in milliseconds).

departures of Group E were at 829, 1625, 2304, 2930, and 3624 ms. There was only one spike at each departure for E6. For E10, there were not only several major spikes at departure but also several small spikes before each major spike. Analysis of the bubble pictures taken from underneath the test section showed that E6 was in the dryout area and E10 was in the vicinity of the contact line of the Group E bubble. E10 had several small heat flux spikes before departure, because it was on edge of the dryout area and was rewet several times as the contact line oscillated with significant transient conduction to the liquid. E6 was in the dryout area, so the oscillations of the contact line had much less effect on the heat transfer on this heater. Thus, there was only one heat flux spike on E6 each ebullition cycle as the bubble started to neck and departed the surface. E6 also had several small spikes before departure during the first two ebullition cycles, because part of the heater was being rewet due to the contact line oscillations during the growth period.

The departure frequencies with coalescence were faster than the departure frequencies during single bubble events. The average departure frequency of the single bubbles on the Group E heaters was 1.35 s^{-1}, whereas the average departure frequency of the bubbles with coalescence was 2.95 s^{-1}, more than twice the bubble departure frequency for the single bubble events. The average growth time for bubbles before coalescence was 160 ms, and the average coalescence-to-departure time was 110 ms, as shown in Figure 12. The coalescence-to-departure period, which had relatively high heat fluxes, accounted for 59% of the total ebullition period. The average growth time for single bubbles on the Group E heaters was 687 ms, whereas the necking-to-departure time was only 12 ms, so the necking-to-departure time, which also had relatively high heat fluxes, accounted for only 1.7% of the total ebullition period during the single bubble events, as shown in Figure 12. The long average coalescence-to-departure times reflected the same size coalescence events with long departure times, during which the average coalescence-to-departure time reached 227 ms while the growth time was only 137 ms, as shown in Figure 12. The same size coalescence with a short departure had an average growth time of 192 ms and a departure time of 46 ms. The growth time in the long departure case was shorter than the growth time in the short departure case, which resulted in smaller bubbles, as they coalesced for the long time to departure cases. The bubble formed after coalescence was then smaller, so it did not immediately depart from the surface resulting in long departure times. The bubbles with the longer growth times were larger when they coalesced so the combined bubble immediately departed the surface.

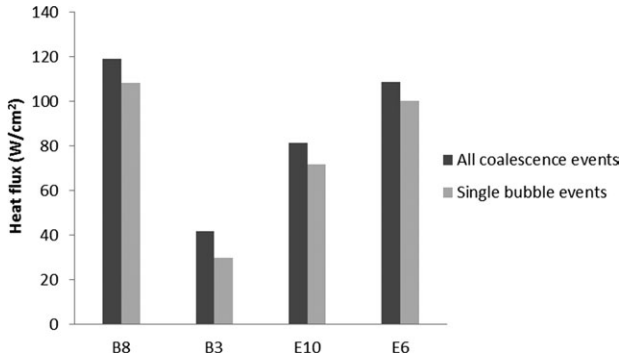

Figure 13. Comparison of maximum heat fluxes for coalescence and single bubble events.

The heat flux increase for each heater due to coalescence and departure during the coalescence events was larger than the heat flux increase due to detachment in the single bubble events, as can be seen in Figure 13. The maximum heat fluxes on B8, B3, E10, and E6 reached 119.1, 42.0, 81.3, and 108.7 W/cm^2 during coalescence events comparing to 108.1, 29.9, 71.7, and 100.2 W/cm^2 during single bubble departure events as shown in Figure 13, indicating the stronger influence of the coalescence. The maximum heat flux for each heater was larger by nearly 10 W/cm^2 during the coalescence events. The increased bubble departure frequency and coalescence to departure time greatly increased the number of heat flux spikes that increased the average heat flux. B8 had the highest average heat flux for both the single bubble and coalescence events. The maximum heat flux increased from 19.8 W/cm^2 during the single bubble events to 33.1 W/cm^2 during the coalescence bubble events, as shown in Figure 14. The average heat flux on E6 during coalescence events was 75% larger than the average heat flux during single bubble events, increasing from 9.6 to 16.8 W/cm^2. The heat flux increases for B3 were smaller, only increasing from 8.2 to 10.7 W/cm^2. E10 had almost the same average heat flux of 8.5 W/cm^2 during the coalescence and single bubble events. B8 had the highest average heat flux, because the heat flux for B8 remained high during all of the long coalescence to departure process due to the rapid formation and collapse of small bubbles on B8 while the E6 and B3 heaters had a series of heat flux spikes as the contact line oscillated across those heaters. E6 had a higher average heat flux than B3, because the microlayer on E6 covered a larger part of the heater. E10 was in the dryout area during the coalescence events, so there were few heat flux spikes on E10 and the average heat flux did not change much. The maximum heat fluxes on all the heaters were only about 10% higher for the coalescent events than for the single bubble events, whereas the average heat fluxes were 75% higher. This implies that the frequency of the heat flux spikes had a much larger influence than the magnitude of the heat flux peaks on the heat flux enhancement.

Conclusions

A microheater array was used to generate bubbles on a constant temperature surface. Bubble coalescence events and single bubble events were observed with CCD cameras with a high-speed data acquisition system measuring the heat fluxes at the same time at different positions underneath the bubble. Four typical heaters were selected to represent different positions under the bubbles, and their heat flux characteristics were interpreted by synchronizing the heat flux measurements and the bubble dynamics seen in the images. The results show that:

1. Four kinds of coalescence events were observed in the experiments with same size coalescence without departure, different size coalescence, same size coalescence with a long time to departure, and same size coalescence with immediate departure. These four kinds of events alternated during the boiling. The heat fluxes for the four different cycles were quite different. Detailed local heat flux variations were analyzed for two typical cycles with the heat fluxes correlated with the bubble dynamics.

2. Bubble stretching and shrinking in two directions were observed after coalescence. The deformation of the bubble interface resulted in oscillations of the contact line observed in the pictures after coalescence. Surface tension forces, the pressure inside the bubble, and liquid momentum are believed to drive the bubble shape oscillations.

3. The heat fluxes for four typical heaters representing different positions under the bubble were analyzed with one heater always outside the dryout areas of both bubbles, one heater between the two bubbles and on the edge of the contact line of the bubbles, one heater always in the dryout area, and one heater right underneath the contact line of one bubble. These four heaters represented the fully wetted regions, regions experiencing transient conduction after rewetting, the moving evaporating microlayer region, and the dryout area. These four regions under the bubble had distinctive heat transfer characteristics. Heaters in the dryout area had only one short heat flux spike at departure, whereas heaters around the contact line had many spikes due to oscillations of the contact line location that resulted in rewetting and movement of the evaporating microlayer across the heater.

4. Detailed analyses of the heat flux characteristics during one bubble ebullition cycle showed that transient conduction due to the movement of the contact line during bubble coalescence, sliding, stretching, and oscillation was the main mechanism resulting in the high heat transfer rates during coalescence events. Microlayer evaporation was also an important mechanism during the coalescence events. Heaters located between the two coalescing bubbles experienced a spike in their heat transfer rates during coalescence due to fast evaporation of the liquid layer trapped between the two bubbles. Heaters underneath the contact line also showed higher heat fluxes as the contact line position oscillated on the heater indicating higher heat transfer rates as the microlayer evaporated.

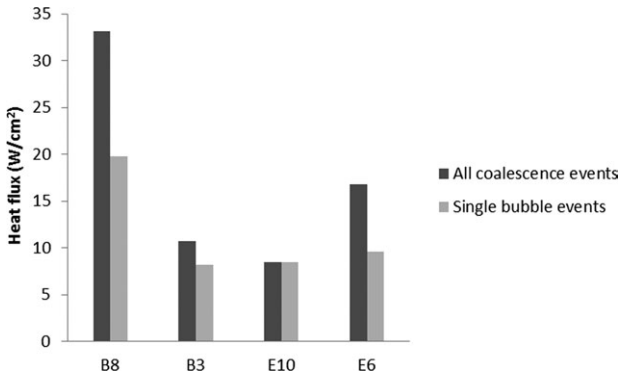

Figure 14. Comparison of average heat fluxes for coalescence and single bubble events.

5. The heat flux enhancement due to bubble coalescence was much larger than the heat flux enhancement due to bubble growth, accounting for nearly 90% of the total heat flux increase. The coalescence to departure time accounted for 59% of the entire ebullition time during coalescence events, so the high heat flux region accounted for a much larger part of the entire ebullition time than for single bubble events. Quantitative analysis of the maximum and average heat fluxes showed that the coalescence enhanced the average heat flux by 75% but only enhanced the maximum heat flux by around 10%. The results show that the increase in the average heat flux was mostly due to the increase of the bubble departure frequencies and the number of heat flux spikes.

Acknowledgments

This work was supported by the National Natural Science Foundation of China, Grant No. 50876050 and the National Basic Research Program of China ("973" Project), Grant No. 2011CB706904.

Literature Cited

1. Golobic I, Petkovsek J, Kenning DBR. Bubble growth and horizontal coalescence in saturated pool boiling on a titanium foil, investigated by high-speed IR thermography. *Int J Heat Mass Transfer*. 2012;55:1385–1402.
2. Golobic I, Petkovsek J, Gjerkes H, Kenning DBR. Horizontal chain coalescence of bubbles in saturated pool boiling on a thin foil. *Int J Heat Mass Transfer*. 2011;54:5517–5526.
3. Chen RH, Tian WX, Su GH, Qiu SZ, Ishiwatari Y, Oka Y. Numerical investigation on coalescence of bubble pairs rising in a stagnant liquid. *Chem Eng Sci*. 2011;66:5055–5063.
4. Studiyo R, Andersson R. Bubble trapping and coalescence at the baffles in stirred tank reactors. *AIChE J*. 2007;53:2232–2239.
5. Perilla JE, Jana SC. Coalescence of immiscible polymer blends in chaotic mixers. *AIChE J*. 2005;51:2675–2685.
6. Dhir VK. Numerical simulations of pool-boiling heat transfer. *AIChE J*. 2001;47:813–834.
7. Stover RL, Tobias CW, Denn MM. Bubble coalescence dynamics. *AIChE J*. 1997;43:2385–2392.
8. Rosenhow WM. A method of correlating heat transfer data for surface boiling of liquids. *Trans ASME* 1952;4:969–975.
9. Forster HK, Zuber N. Dynamics of vapor bubbles and boiling heat transfer. *AICHE J*. 1955;1:531–535.
10. Mikic BB, Rohsenow WM, Griffith P. On bubble growth rates. *Int J Heat Mass Transfer*. 1969;13:657–666.
11. Moore FD, Mesler RB. The measurement of rapid surface temperature fluctuations during nucleate boiling of water. *AIChE J*. 1961; 7:620–624.
12. Hendricks RC, Sharp RR. Initiation of cooling due to bubble growth on a heating surface. NASA Report TND2290, 1964.
13. Cooper MG, Lloyd AJP. Microlayer in nucleate pool boiling. *Int J Heat Mass Transfer*. 1969;12:895–913.
14. Stephan P, Hammer J. A new model for nucleate boiling heat transfer. *Warme und Stoffubertragung*. 1994;30:119–125.
15. Moghaddam S, Kiger K. Physical mechanisms of heat transfer during single bubble nucleate boiling of FC-72 under saturation conditions. Experimental investigation. *Int J Heat Mass Transfer*. 2009; 52:1284–1294.
16. Moghaddam S, Kiger K. Physical mechanisms of heat transfer during single bubble nucleate boiling of FC-72 under saturation conditions. Theoretical analysis. *Int J Heat Mass Transfer*. 2009;52:1295–1303.
17. Christopher DM, Wang H, Peng XP. Dynamics of bubble motion and bubble top jet flows from moving vapor bubbles on microwires. *J Heat Transfer*. 2005;127:1260–1268.
18. Zhang L, Shoji M. Nucleation site interaction in pool boiling on the artificial surface. *Int J Heat Mass Transfer*. 2003;46:513–522.
19. Bonjour JM, Clausse M, Lallemand M. Experimental study of the coalescence phenomenon during nucleate pool boiling. *Exp Therm Fluid Sci*. 2000;20:180–187.
20. Siedel S, Cioulachtjian S, Bonjour J. Experimental analysis of bubble growth, departure and interactions during pool boiling on artificial nucleation sites. *Exp Therm Fluid Sci*. 2008;32:1504–1511.
21. Coulibaly A, Christopher DM. Effect of bubble coalescence on the wall heat transfer during subcooled pool boiling. *Exp Therm Fluid Sci*. http://dx.doi.org/10.1016/j.expthermflusci.2012.06.010.
22. Demiray F, Kim J. Microscale heat transfer measurements during pool boiling of FC-72: effect of subcooling. *Int J Heat Mass Transfer*. 2004;47:3257–3268.
23. Christopher DM, Jiang J. Bubble sweeping and interactions on wires during subcooled boiling. *Int J Heat Mass Transfer*. 2009;52:5020–5028.
24. Chen T, Chung JN. Coalescence of bubbles in nucleate boiling on microheaters. *Int J Heat Mass Transfer*. 2002;45:2329–2341.
25. Lin XP, Christopher DM. *Bubble growth during nucleate boiling in microchannels*. In: *Proceedings of the 14th International Heat Transfer Conference, IHTC14-22725*, Washington, 2010.
26. Li D, Dhir VK. Numerical study of a single bubble sliding on a downward facing heated surface. *J Heat Transfer*. 2007;129: 877–883.
27. Ma HB, Cheng P, Borgmeyer B, Wang YX. Fluid flow and heat transfer in the evaporating thin film region. *Microfluid Nanofluid*. 2008;4:237–243.

Manuscript received May 21, 2012, and revision received Aug. 16, 2012.